symmetry

MDPI

Article

Annealing Effects on Microstructure and Texture in KOBO-Processed LPBF AlSi10Mg Alloy: Elucidating CSL Boundary Formation

Przemysław Snopiński [1,*], Lovro Liverić [2] and Juraj Beniak [3]

[1] Department of Engineering Materials and Biomaterials, Faculty of Mechanical Engineering, Silesian University of Technology, 44-100 Gliwice, Poland
[2] Faculty of Engineering, Centre for Micro- and Nanosciences and Technologies, University of Rijeka, Vukovarska 58, 51000 Rijeka, Croatia; lovro.liveric@riteh.uniri.hr
[3] Faculty of Mechanical Engineering, Slovak University of Technology in Bratislava, Nam. Slobody 17, 81231 Bratislava, Slovakia; juraj.beniak@stuba.sk
* Correspondence: przemyslaw.snopinski@polsl.pl

Abstract: This study introduces a strain-annealing approach to tailor the grain boundary characteristics of additively manufactured AlSi10Mg alloy produced by Laser Powder Bed Fusion (LPBF). By combining KOBO extrusion and subsequent annealing treatments, we aim to increase the proportion of low-Σ coincident site lattice (CSL) grain boundaries, particularly Σ3 boundaries. Through grain boundary engineering (GBE), specifically focused on inducing a high fraction of symmetrical CSL boundaries, our approach allows for the optimization of microstructural features that inhibit defect propagation and improve material stability. Microstructural analysis using electron backscatter diffraction (EBSD) revealed a substantial increase in Σ3 boundaries (60° <111> twin relationship) in the early recrystallization stages of the KOBO-processed LPBF AlSi10Mg alloy, demonstrating the effectiveness of this method. The findings presented in this manuscript highlight a new strategy for advancing the microstructural characteristics of LPBF AlSi10Mg alloy, with promising implications for applications requiring high-performance materials, such as in the aerospace, nuclear, and automotive industries.

Keywords: grain boundary engineering; AlSi10Mg alloy; microstructure; CSL boundaries; texture analysis

check for updates

Citation: Snopiński, P.; Liverić, L.; Beniak, J. Annealing Effects on Microstructure and Texture in KOBO-Processed LPBF AlSi10Mg Alloy: Elucidating CSL Boundary Formation. *Symmetry* **2024**, *16*, 1663. https://doi.org/10.3390/sym16121663

Academic Editors: Sergei Odintsov, Vasilis K. Oikonomou and Luigi Nicolais

Received: 25 September 2024
Revised: 21 November 2024
Accepted: 13 December 2024
Published: 16 December 2024

Copyright: © 2024 by the authors. Licensee MDPI, Basel, Switzerland. This article is an open access article distributed under the terms and conditions of the Creative Commons Attribution (CC BY) license (https://creativecommons.org/licenses/by/4.0/).

1. Introduction

The AlSi10Mg alloy is highly valued in additive manufacturing for its unique properties. Its high specific strength and low density make it ideal for lightweight, load-bearing applications in the aerospace and automotive sectors, where weight reduction is crucial [1]. Additionally, the silicon in AlSi10Mg provides corrosion resistance, helping it withstand harsh environments. Its near-eutectic composition also contributes to a lower melting point and enhanced fluidity, making it well-suited for additive manufacturing processes like Laser Powder Bed Fusion (LPBF) that demand precise melting and solidification control [2,3].

In the as-cast condition, AlSi10Mg alloy has a dendritic structure, with Si and Mg_2Si precipitates. However, in LPBF, ultrafast cooling rates (10^3–10^6 °C/s) produce a multi-level heterogeneous microstructure due to repeated melting and cooling cycles [4–7]. The microstructure features semicircular melt pools (parallel to the build direction) or laser scan traces (perpendicular to the build direction), leading to a varied grain size distribution. Smaller grains form at melt pool (MP) boundaries, while larger grains are inside. Additionally, the Si phase morphology differs, with isolated Si precipitates at MP borders and coarse and fine Al/Si cells within, which is key to LPBF materials' unique properties [5,8].

LPBF AlSi10Mg parts often undergo post-processing, categorized into "bulk" treatments like heat treatment and surface treatments. Heat treatments, such as T6 or direct

aging, primarily aim to enhance mechanical properties. For instance, Di Egidio et al. [9] demonstrated that rapid solution (10 min at 510 °C) followed by aging (6 h at 160 °C) can yield a UTS of 319 MPa and 12.6% elongation. Zhang et al. [10] showed that direct aging increased tensile strength from 403 to 451 MPa with 6.5% elongation. Surface treatments like sandblasting [11], shot peening [12], and water jet processing [13] introduce compressive stresses to improve fatigue resistance.

Less common post-processing methods for LPBF parts are those based on plastic deformation, such as hot isostatic pressing [14,15] or Ampliforge™ [16]. However, despite the beneficial influence on ductility, these techniques cause a deterioration of mechanical properties, as has been shown in several articles [17–19].

Avant-garde post-processing treatments employ severe plastic deformation (SPD), the aim of which is to impose high shear deformation to produce an ultrafine grained and/or nanocrystalline microstructure [20]. The SPD of LPBF parts focuses on "defect engineering" with the aim of achieving exceptional properties that cannot be obtained using conventional methods. For example, using the high-pressure torsion (HPT) method, it has been shown that it is possible to refine the grains of LPBF 316L steel to the nanometer regime (average grain size 42 nm) while simultaneously improving the nano hardness of the alloy by approximately 100% [21]. Similarly, the Equal Channel Angular Pressing method has been shown to effectively improve the mechanical properties of Al-Si alloys, as described in [22].

A very recent strategy aimed at improving the properties of LPBF parts is grain boundary engineering (GBE). The goal of GBE is to increase the fraction of low-ΣCSL boundaries, such as Σ3, Σ3n (n > 1) twin boundaries (TB), and optimize grain boundary character distribution (GBCD) [23]. TBs can be classified into two types: (i) coherent and (ii) incoherent. Coherent twins usually exhibit mirror-like symmetry and very low interfacial energy, while incoherent twins exhibit higher interfacial energy than coherent twins but lower than random grain boundaries [24]. Typically, GBE involves several iterations of cold deformation followed by annealing treatment, and thus it can be easily applied for conventional materials. There is great interest in GBE because GBE materials exhibit superior properties, such as improved intergranular corrosion resistance, oxidation resistance, creep resistance, and excellent ductility. For example, Zhang et al. [25] investigated the effect of GBE on intergranular corrosion of the Ni-Cr-Mo-based C276 superalloy and revealed that samples with a higher fraction of CSL boundaries exhibited greater corrosion resistance compared to those with a lower fraction of CSL boundaries. Improved oxidation resistance has been demonstrated, for example, in the Ni-based superalloy 617, investigated by Athreya et al. [26]. Zhang et al. [27] revealed the beneficial influence of GBE treatment and special grain boundary networks on the creep resistance of the NiCoCr alloy. Additionally, the favorable effect of CSL boundary networks on ductility has been shown for numerous alloys, as highlighted in several studies [23,28–30].

While conventionally manufactured materials often undergo repeated deformation and annealing, the LPBF technique is used to produce parts with precise dimensions and tolerances from the outset. Subjecting these parts to additional "bulk" deformation could compromise their intended geometry and functional performance. Therefore, post-processing strategies typically applied to traditional alloys may not be directly applicable to or advantageous for LPBF-manufactured parts.

For this reason, scientists have proposed alternative strategies to improve the fraction of CSL boundaries in LPBF materials. The first, applied especially for low SFE materials, is a so-called "direct GBE". Direct GBE means that the high stored energy (mainly in the form of geometrically necessary dislocations whose density in LPBF-produced metal alloys ranges between 10^{13} m^{-2} and 10^{14} m^{-2}) is transformed into an advantage to obtain low CSL boundaries through direct heat treatment, without any plastic deformation preprocessing. In principle, the residual strain within the grains (usually manifested as misorientation gradients) should be sufficient to initiate recrystallization at temperatures typical of industrial processes, without the need for additional plastic deformation. However, studies have

demonstrated that additively manufactured alloys remain thermally stable even at relatively high annealing temperatures. For example, in the study of Liu et al. [31] it has been reported that the Inconel 718 alloy remains thermally stable up to 1100 °C. As indicated by Gao et al. [32], the thermal stability of additively manufactured alloys is attributed to the presence of distinctive cellular solidification structures. Research indicates that this structure inhibits the initiation and development of recrystallization, despite the presence of a driving force, such as geometrically necessary dislocations (GNDs), within the microstructure. However, some reports indicate the effectiveness of this strategy in improving the CSL boundary fraction. For example, in the study of Zhang et al. [33] it was shown that heat treatment of the LPBF CoCrMo alloy resulted in an increase in the 60° <111> boundary fraction of up to about 25%. Similarly, Liu et al., who studied direct-GBE in LPBF Inconel 718, reported an increase in the Σ3 twin boundary fraction from 0.4% to 64.89% when the alloy was subjected to annealing at 1200 °C.

The second strategy aims to induce simultaneous deformation and recrystallization of the bulk material in one step. This strategy has been used, for example, to post-process 304L austenitic steel [34]. In this study, the LPBF alloy was subjected to hot isostatic pressing (HIP). The twin boundary fraction was found to increase to approximately 73% in the HIPed state after straining. This strategy was also shown to be effective in a study of Inconel 718 [35], in which the authors reported a twin boundary fraction of approximately 66%.

Another recent strategy discussed in the literature is the development of a so-called "programmable microstructure". This approach creates regions of varying dislocation density, which are "programmed" during the LPBF process. This means that the strain required for recrystallization-based GBE is inherently generated during fusion-based additive manufacturing [36].

Upon reviewing the existing research, we found that GBE strategies predominantly focus on low- to medium-SFE materials, with limited attention given to their application in high-SFE materials, such as aluminum alloys. The unique characteristics of these alloys, particularly their higher SFE and cellular microstructure, present distinct challenges and opportunities for GBE. Thus, exploring the adaptation and effectiveness of GBE strategies for high-SFE materials could provide valuable insight and potentially drive significant advancements in materials science.

As mentioned above, the typical grain boundary engineering (GBE) strategy for LPBF alloys involves direct GBE, which generally requires the presence of misorientation gradients in the microstructure. These gradients serve as the driving force for recrystallization during both the LPBF process and post-LPBF heat treatment. In LPBF alloys, misorientation gradients refer to variations in crystallographic orientation between adjacent cellular structures and grains. Multiple studies [37–39] have shown that LPBF aluminum alloys exhibit smaller grains with lower misorientation gradients compared to alloys such as LPBF stainless steel [40].

In LPBF aluminum alloys, rapid heat dissipation during the LPBF process can limit the extent of thermal gradients and the associated residual stresses. As a result, the direct GBE strategy may be less effective due to the significantly lower driving force for recrystallization. Additionally, the unique cellular microstructure has been shown to inhibit the initiation and growth of recrystallization nuclei. For this reason, alternative strategies must be developed to activate recrystallization and promote the formation of twin boundaries (TBs) in high stacking fault energy (SFE) aluminum alloys. This strategy, developed for 316L steel, involves the "weakening" of this distinctive solidification structure [32]. Another interesting strategy has recently been introduced by the author of this manuscript. This strategy incorporates the bulk deformation that is achieved by KOBO extrusion [41]. Although this approach may seem counterintuitive for LPBF parts, since it compromises one of the key advantages of additive manufacturing—-the ability to produce components that are nearly net-shaped—-it could effectively modify the grain boundary character distribution. This strategy is based on the assumption that the driving force for the migration of the grain boundary arises from the stored energy difference between {111}

and {100} grains. That is, grains with {100}//ND fiber texture carry less stored energy compared to grains with {111}//ND texture after deformation. During such migration, the grain boundary moves from the grain with a lower Schmid factor and a higher Taylor factor to the grain with a higher Schmid factor and a lower Taylor factor [42].

The first results documenting the microstructural evolution and the potential in improving the low Σ CSL boundary fraction in LPBF AlSi10Mg aluminum alloy were published in [43]. Based on this, a subsequent study [41] focused on investigating the annealing phenomenon at a wide range of temperatures. Although the study provided valuable information on microstructure evolution, it reported only a minor improvement in the CSL boundary fraction. The article builds on previous work, aiming to further enhance the effectiveness of the strain-annealing route to improve the low-Σ CSL boundary fraction and advance the use of the KOBO extrusion process for fabricating materials with unique properties. Notably, this study introduces a refined methodology that combines controlled strain with precise thermal cycles, setting it apart by offering a systematic approach to maximizing CSL boundary formation. Additionally, the detailed texture evolution analysis provided here is intended to elucidate the mechanisms governing the increase in the low-ΣCSL boundary fraction, contributing novel insights into texture-engineering strategies for LPBF alloys.

2. Research Methodology

Aluminum-magnesium-silicon alloy powder with a mean particle size of 60 µm was used to produce 99.7% dense parts via LPBF. The nominal chemical composition of the powder is given in Table 1.

Table 1. The nominal chemical composition of the AlSi10Mg alloy powder used to fabricate the LPBF samples.

Al	Si	Mg	Ti	Cu	Fe
87.8	10.5	0.5	0.15	0.15	0.09

Samples were produced using a TruPrint LPBF system (Trumpf, Ditzingen, Germany) equipped with a ytterbium fiber laser. Before the printing process started, the printing chamber was flooded with argon to reach an oxygen level below 0.02%. The following LPBF process parameters were used:

- Laser power = 175 W
- Layer thickness = 20 µm
- Scan speed = 1400 mm/s
- Scanning strategy = zigzag with a rotation of 67 degrees.

The sample, with a diameter of 60 mm and a height of 50 mm, was subjected to KOBO extrusion. The following process parameters were used in order to obtain an extrusion ratio of λ = 225, resulting in a reduction in diameter from 60 mm to 8 mm:

- Die oscillation frequency of 5 Hz
- Die angle oscillation equal to ±8°
- punch speed 0.2 mm/s
- True strain = 5.42.

Subsequently, the as-built and KOBO-processed samples were annealed in a resistance furnace at 500 °C for 1, 2, and 3 h under an argon atmosphere.

Samples for microstructural analysis were prepared conventionally, according to well-known metallographic procedures, including mounting in an epoxy resin, grinding with water SiC papers, and polishing with 3 µm and 1 µm diamond pastes. In order to improve the surface quality, a final polishing was performed using a SiC colloidal suspension for 1 h.

Grain size and crystallographic orientation information were acquired using a Zeiss Supra 35 scanning electron microscope (Carl Zeiss NTS GmbH, Oberkochen, Germany) equipped with an electron backscatter diffraction detector. EBSD maps were collected with the following parameters:

- Accelerating voltage of 20 kV
- Working distance of 15 mm
- Step size of 0.4 for the as-built sample, 0.08 for the KOBO-processed sample, and 0.1 for the KOBO-processed and annealed sample.

All EBSD scans were performed on the ND-TD plane.

The EBSD data were then analyzed using TSL-OIM (version 7.3.1) and ATEX (version 4.15) software [44]. The following cleanup procedure involving correlation of neighboring grains and standardization of the grain confidence index was applied to the EBSD data:

- Minimum confidence index of 0.1
- Grain misorientation angle 5°
- Grains smaller than 9 pixels were excluded from the EBSD analysis.

With the aim to identify the CSL boundaries, the Brandon criterion was used. For example, in order to identify the CSL-Σ3 boundaries, the maximum deviation was set as 8.7°. To analyze the recrystallized volume fraction, the following criteria were applied:

- Minimum grain size of 9 pixels
- Grain orientation spread < 1 degree.

The recrystallized fraction was determined by classifying the grains into recrystallized and nonrecrystallized categories based on their grain orientation spread (GOS) values. The grain orientation spread (GOS) for each grain is generally determined by calculating the deviation between the average orientation of the grain and the crystal orientation of individual points within the grain. Recrystallized grains typically exhibit low GOS values because of their uniform orientation, whereas deformed or partially recrystallized grains show higher GOS values. A critical GOS threshold (GOS < 1°) was established through a literature review and preliminary analysis. Grains with GOS values below this threshold were classified as recrystallized, while those with higher GOS values were considered nonrecrystallized. The recrystallized fraction was calculated from the ratio of the area of recrystallized grains to the total area of all grains in the analyzed region, according to the following formula:

$$Recrystallized\ fraction = \frac{Number\ of\ recrystallized\ grains}{Total\ number\ of\ grains} \quad (1)$$

Since the samples were sectioned perpendicular to the extrusion direction, for the quantitative texture evolution analysis the EBSD data were rotated according to the following procedure. First, the orientation matrix was rotated α around ND, and then a new orientation matrix was rotated β around TD to align the ED horizontally and TD vertically. Then, the ODFs were plotted to provide a comprehensive description of the texture. Multiples of a random distribution (MRD) were calculated to quantify the strength of the texture. An MRD value greater than 1 indicated a preferred orientation, with higher values signifying stronger textures.

Vickers microhardness (HV) measurements were taken on the cross-sectional plane using a microhardness testing device manufactured by Future-Tech (Future-Tech Corp. Tokyo, Japan). A load of 100 gf was applied at each indentation, with a dwell time of 15 s. For each sample, ten measurements were performed.

3. Results

3.1. Microstructure Characterization of the As-Built Sample

First the microstructure of the as-built AlSi10Mg alloy sample was characterized. Figure 1a shows the IPF-Z map taken in the XY plane, where the twin-related Σ3n CSL

boundaries (Σ3, Σ9, and Σ27) are marked in white, green, and black, respectively. It reveals a heterogeneous microstructure composed of grains with sizes ranging from approximately 0.6 μm in the scan trace boundary zone (highlighted by white dashed lines) to several micrometers in the scan trace interior. Furthermore, it shows that the as-built sample microstructure exhibit a very low proportion of twin-related Σ3n CSL boundaries, with Σ3, Σ9, and Σ27 boundaries accounting for 2%, 0.9%, and 0.3%, respectively. Since no comparable data for LPBF AlSi10Mg alloys are available in the literature, it is challenging to directly relate these findings to other studies. However, in low-SFE materials, the fraction of low CSL boundaries is significantly higher than that observed in the LPBF AlSi10Mg alloy analyzed here, as reported in [45,46].

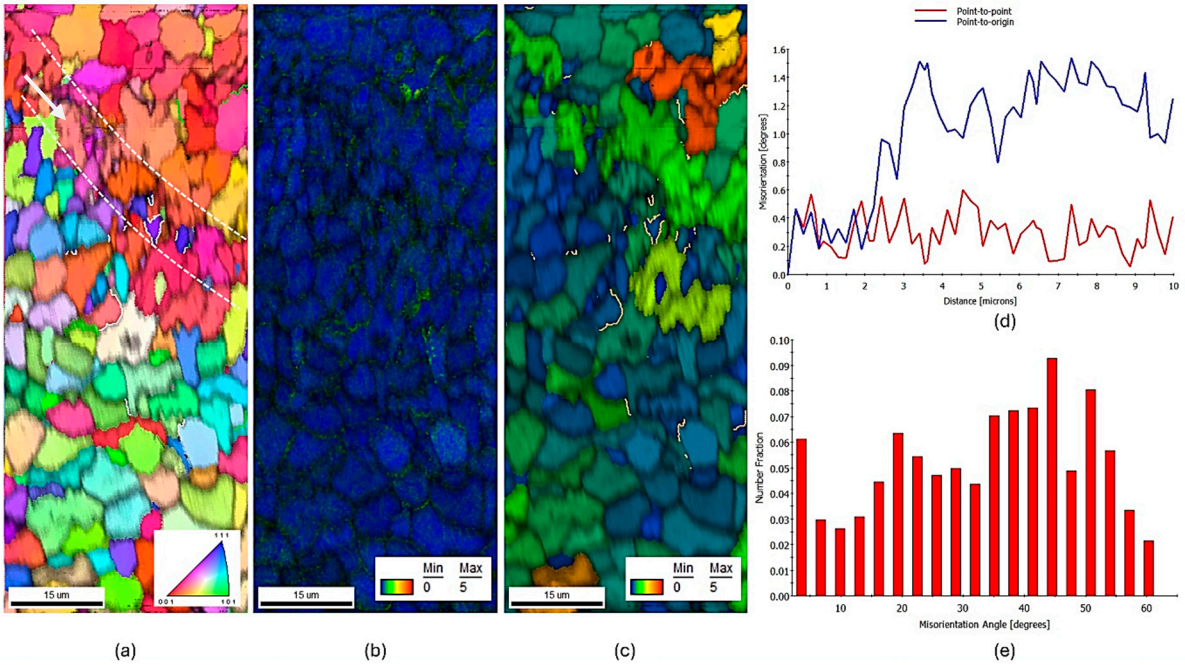

Figure 1. Results of the EBSD analysis for the as-built sample. (**a**) IPF-Z map showing the distribution of twin-related Σ3n CSL, (**b**) the corresponding kernel average misorientation (KAM) map, (**c**) grain orientation spread map in which twin-related Σ3n CSL boundaries are marked in orange color, (**d**) point-to-point misorientation change measured across the white arrow in (**a**), (**e**) histogram of grain boundary distribution.

The local strains were then analyzed by plotting the average kernel misorientation maps. As can be seen in Figure 1b, higher KAM values appear to be localized near some grain boundaries. It is also clear that the KAM value decreases with increasing distance from a boundary to the interior of a grain, suggesting negligible stain localization within the grain area. Furthermore, when examining the change in misorientation across a grain (see white arrow), it is found that an accumulated misorientation angle is quite low, in the range of 1° to 2° (Figure 1d). This implies that the Al/Si cells exhibit a relatively uniform orientation across the grain, which does not require accommodation by geometrically necessary dislocations (GNDs). It can be concluded that most of the dislocations were eliminated as a result of in situ tempering (recovery process) that occurred during melting of the subsequent layer.

Subsequently, the recrystallized fraction was analyzed by plotting the GOS map. As presented in Figure 1c, most of the equiaxed grains are blue and green and have low GOS values, which indicates that these grains did not accommodate large amounts of residual strain during the manufacturing process. Accordingly, in the as-built condition the Rx grains constitute about 92.6% of the total grain fraction area. Furthermore, it is also evident that most of the low-ΣCSL boundaries are located in these Rx regions, indicating that the

LPBF remelting cycles and accompanying microstructure recovery [47] (being in favor of dynamic recrystallization due to heat release) allowed the twins to grow in these areas, probably through boundary migration. The histogram of grain boundary misorientation clearly shows that high-angle boundaries dominate the microstructure, and their fraction constitutes about 80% (Figure 1e).

3.2. Effect of Annealing on Microstructure of As-Built Sample

In the second stage of the experiment, the annealing response of the as-built sample was investigated. The grain boundary maps in Figure 2 and the corresponding histogram of grain boundary misorientation in Figure 3 indicate that high-angle grain boundaries (HAGBs) account for a large fraction of the total GBs. Notably, after annealing for 1 h, the fraction of low-angle grain boundaries (LAGBs) increased from approximately 20% in the as-built condition (Figure 1e) to around 40%. According to Mei et al. [48], this increase in LAGBs can be attributed to sub-grain formation. After annealing for 2 h, the LAGB fraction decreased to about 22%, likely due to migration and merging of LAGBs, which suggests partial recovery or recrystallization during the annealing treatment. Extending the annealing time to 3 h did not significantly alter the LAGBs fraction, which remained at a similar level to that observed in the 2 h sample.

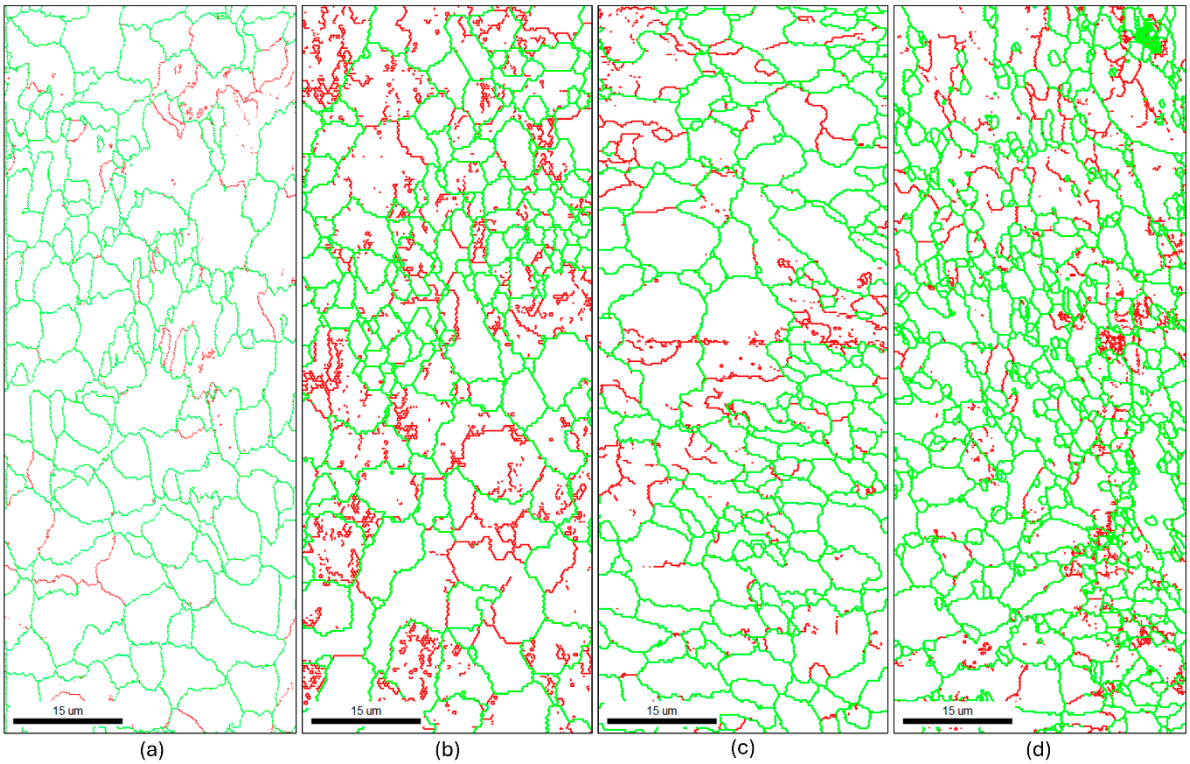

Figure 2. Grain boundary maps for the AlSi10Mg alloy. (**a**) As-built sample, (**b**) as-built and annealed at 500 °C for 1 h, (**c**) as-built and annealed at 500 °C for 2 h, and (**d**) as-built and annealed at 500 °C for 3 h (red—low-angle grain boundaries, green—high-angle grain boundaries).

The effect of annealing on the low-ΣCSL boundary fraction was analyzed, as shown in the histograms in Figure 4. In the as-built sample, twin-related Σ3n CSL boundaries accounted for ~3% of the total boundary fraction. Annealing did not significantly alter the grain boundary character distribution (GBCD); therefore after annealing for 1 h, Σ3, Σ9, and Σ27 boundaries accounted only for approximately 2%, and further increasing the annealing time had a minimal impact on GBCD. The most notable increase occurred after 3 h, where Σ3, Σ9, and Σ27 boundaries rose to about 5% of the total boundary fraction. Overall, the low-ΣCSL boundary fraction remained low, at around 10%.

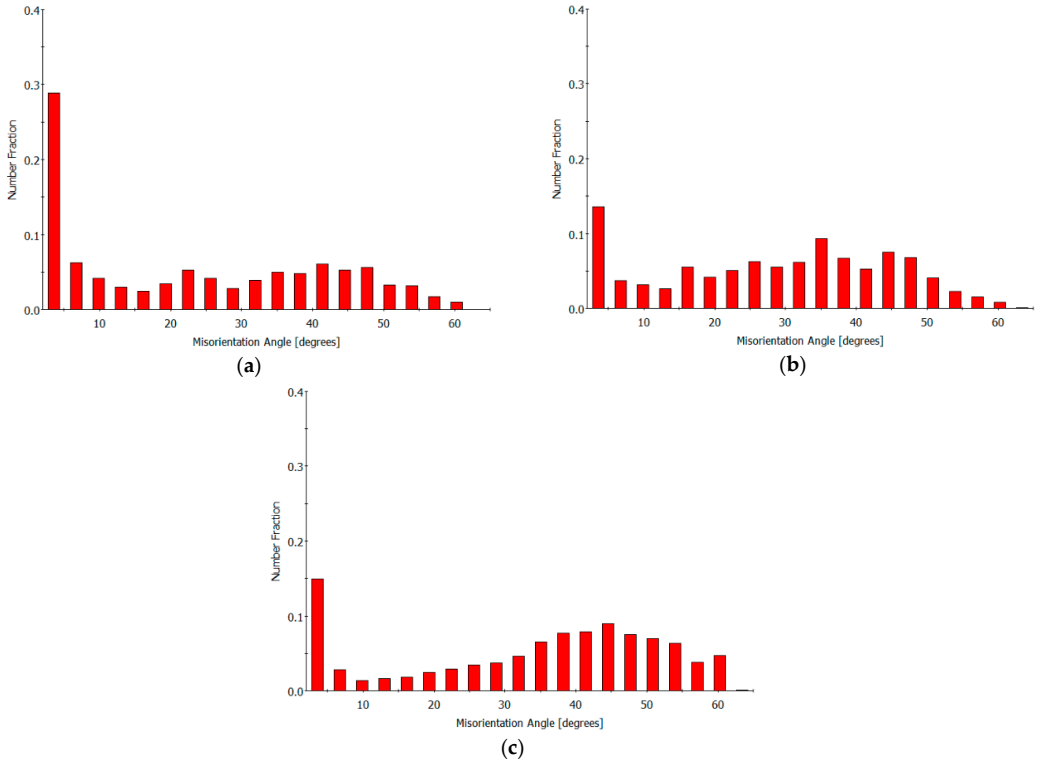

Figure 3. Grain boundary misorientation histograms for the AlSi10Mg alloy. (**a**) As-built sample, (**a**) as-built and annealed at 500 °C for 1 h, (**b**) as-built and annealed at 500 °C for 2 h, and (**c**) as-built and annealed at 500 °C for 3 h.

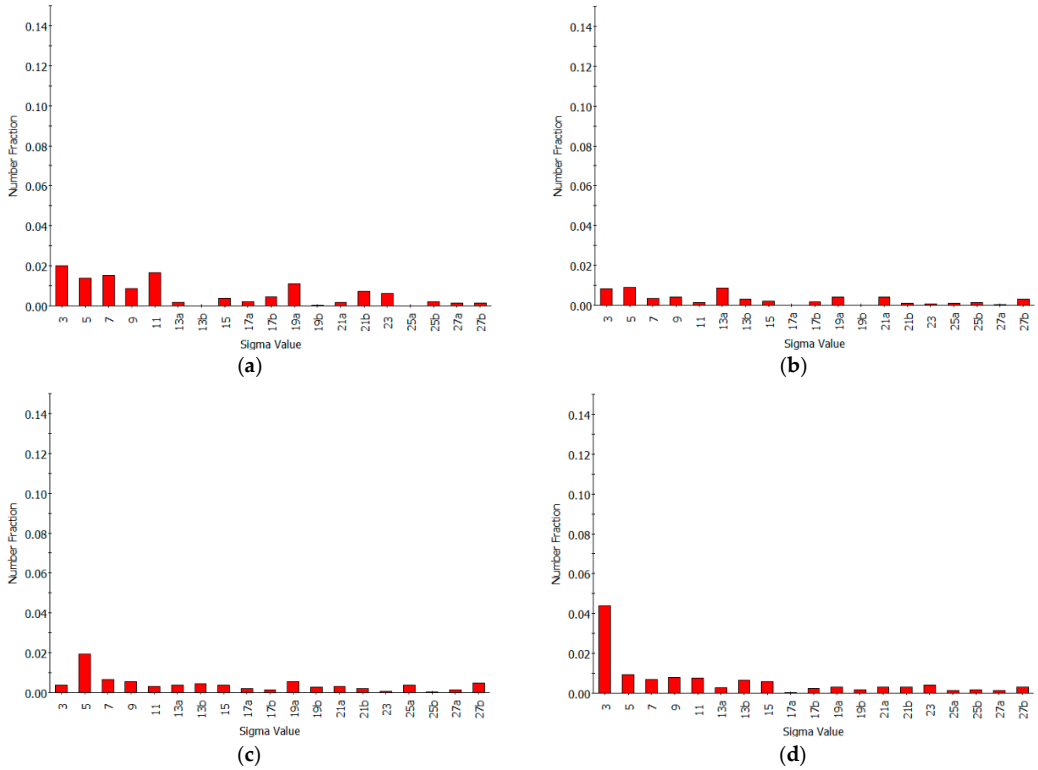

Figure 4. CSL boundary distribution histograms for the AlSi10Mg alloy. (**a**) As-built sample, (**b**) as-built and annealed at 500 °C for 1 h, (**c**) as-built and annealed at 500 °C for 2 h, and (**d**) as-built and annealed at 500 °C for 3 h.

3.3. Microstructure Characterization of the KOBO-Processed Sample

Figure 5 shows the results of the EBSD analysis of the KOBO-processed sample. As can be seen in the IPF-Z map (Figure 5a), the heterogeneous microstructure present in the as-built condition was transformed into a more homogeneous microstructure, in which equiaxed grains with an average size of about 0.8 µm dominated. Furthermore, it is evident that the fraction of twin-related Σ3n CSL boundaries increased slightly compared to the as-built condition. More specifically, the fraction of Σ3 boundaries increased from 3.2% to 7.5%. The histogram of the grain boundary distribution clearly shows a narrow peak at 60° that originates from the Σ3 CSL boundaries. Furthermore, a smaller peak appears at around 40° which may originate from Σ9 CSL boundaries with 39°/<110> misorientation.

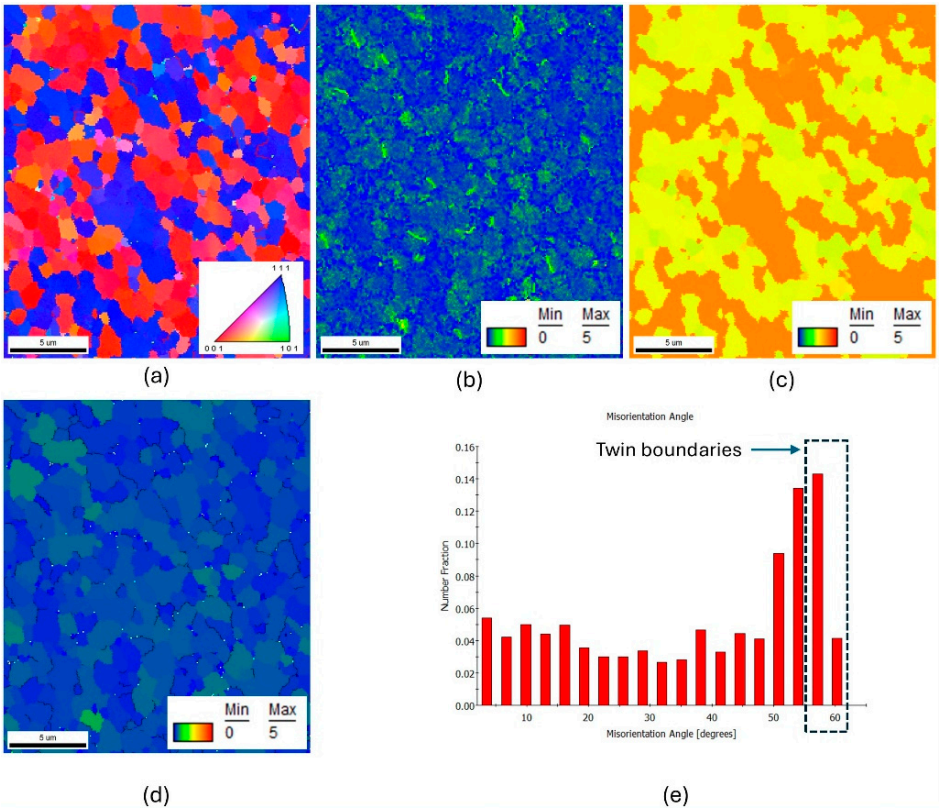

Figure 5. Results of the EBSD analysis for the KOBO-processed sample. (**a**) IPF-Z map showing the grain microstructure and the distribution of low-Σ CSL boundaries, (**b**) the corresponding kernel average misorientation (KAM) map, (**c**) the Taylor factor map for the <111> and <100> grains, (**d**) the grain orientation spread map, and (**e**) a histogram of the grain boundary distribution.

According to the KAM map (Figure 5b), certain grains exhibit higher KAM values and GND density compared to other grains. Furthermore, there is a minor difference between the GND density between <111> and <100> oriented grains. The measured average KAM values for <111> and <100> grains are 0.67 and 0.62, respectively. This difference arises from the accommodation of lattice curvature resulting from differential grain rotations.

The Taylor factor map for <111> and <100> fiber confirms that <111> grains exhibit a relatively higher Taylor factor than <100> grains (Figure 5c). Specifically, the Taylor factor calculated for <111> grains is 3.3, while for <100> grains it is 2.7. A higher Taylor factor indicates that the <111> grains accumulated more deformation energy, which may act as the driving force of grain boundary migration if a suitable annealing treatment is applied. The GOS map in Figure 5d reveals that the Rx grains constitute about 74% of the total grain fraction, which clearly evidences the occurrence of DRX during the extrusion process.

3.4. Effect of Annealing on Microstructure and Texture Evolution of KOBO-Processed Sample

Figure 6 shows the grain size maps for the KOBO-processed and annealed samples. As can be seen, the KOBO-processed sample exhibits the finest grain structure. In this condition, blue grains with sizes between 0 and 2 μm constitute approximately 82% of the total grain population, while green grains within the 2–4 μm range represent the remaining 18% (Figure 6a).

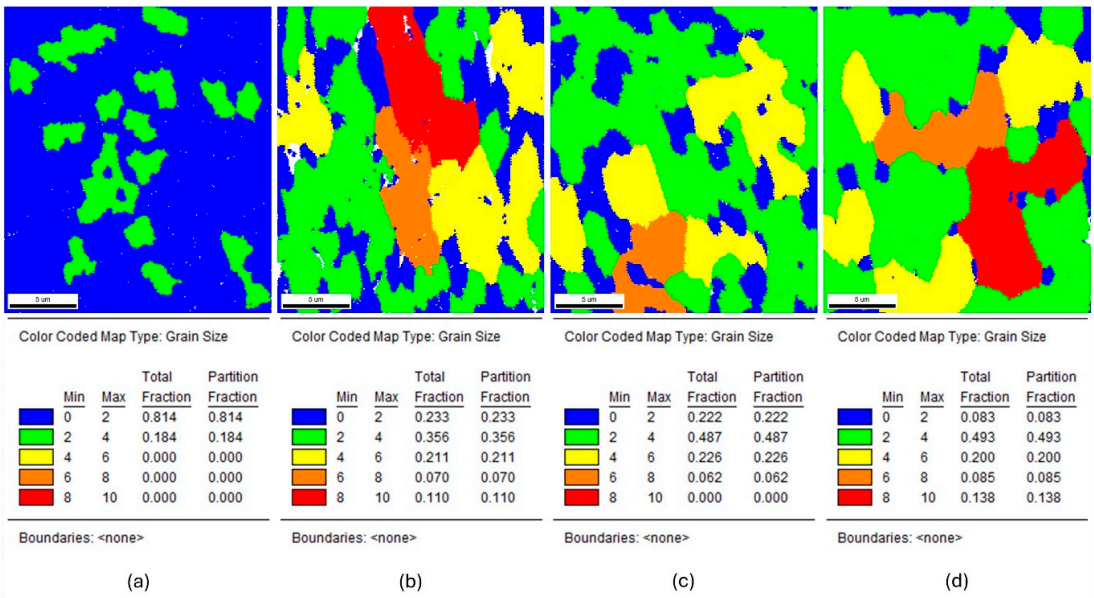

Figure 6. Grain size maps of (**a**) KOBO-processed, (**b**) KOBO-processed and annealed at 500 °C for 1 h, (**c**) KOBO-processed and annealed at 500 °C for 2 h, and (**d**) KOBO-processed and annealed at 500 °C for 3 h samples.

After annealing at 500 °C for 1 h, the grain size distribution became more varied (Figure 6b). Grains within the 0–2 μm range were reduced to 23%, while a notable increase occurred in the 2–4 μm range, comprising 35% of the total grains. Additionally, larger grain populations emerged, with 21% of grains falling between 4 and 6 μm, 7% between 6 and 8 μm, and 11% in the 8–10 μm range, reflecting grain growth processes initiated during the early stages of annealing.

After 2 h of annealing, a continued trend of grain coarsening was observed, as seen in Figure 6c. The proportion of grains in the 0–2 μm range slightly decreased to 22%, while the fraction of 2–4 μm grains substantially increased to 49%. Grains within the 4–6 μm range accounted for 23%, and those between 6 and 8 μm represented 6% of the population, indicating ongoing grain boundary migration and growth during the extended annealing period.

Finally, after 3 h of annealing, pronounced grain coarsening was observed, as illustrated in Figure 6d. The proportion of grains within the 0–2 μm range significantly dropped to 8%, while the 2–4 μm fraction remained constant at 49%. Grains in the 4–6 μm range accounted for 20%, and the presence of larger grains in the 6–8 μm and 8–10 μm ranges increased to 8% and 14%, respectively. This prolonged annealing appears to further facilitate grain growth, resulting in a more heterogeneous grain structure with a greater prevalence of larger grains.

After analyzing the grain size, the grain boundary distribution was quantitatively characterized. Figure 7 shows the grain boundary maps along with the corresponding misorientation histograms. According to grain boundary misorientation histogram, LAGBs constitute approximately 19% of the total grain boundary fraction, with HAGBs accounting for the remaining 81% in the KOBO-processed sample (Figure 7a). After annealing for 1 h (Figure 7b), dislocations within the cell walls reorganized to form distinct low-angle boundaries between adjacent cells. Consequently, the grain boundary map reveals an increase in

the fraction of LAGBs to approximately 40%. This increase in the LAGB fraction can be attributed to recovery processes. During recovery, dislocations within the highly deformed microstructure rearrange, forming stable subgrain structures delineated by LAGBs. This formation of subgrains reflects the system's tendency to reduce internal strain energy by organizing dislocations into lower-energy configurations. After 2 h of annealing, a decrease in the LAGB fraction was noted, likely due to the onset of recrystallization (Figure 7c). This process replaces LAGBs with high-angle grain boundaries (HAGBs) as new grains nucleate and grow, reducing the overall fraction of LAGBs within the microstructure. Interestingly, after annealing for 3 h, the LAGB fraction increased (Figure 7d). This may be associated with the growth of second-phase particles, which can exert a Zener pinning effect on the grain boundaries. With partially reduced Zener pinning, some grain boundaries become more mobile, allowing for boundary migration and growth in some regions. However, in regions with lower dislocation density or fewer driving forces for recrystallization, subgrain structures with LAGBs may persist as a stable configuration. This can lead to a dynamic equilibrium where some grain boundaries evolve into HAGBs, while others remain as LAGBs due to local variations in energy and boundary mobility.

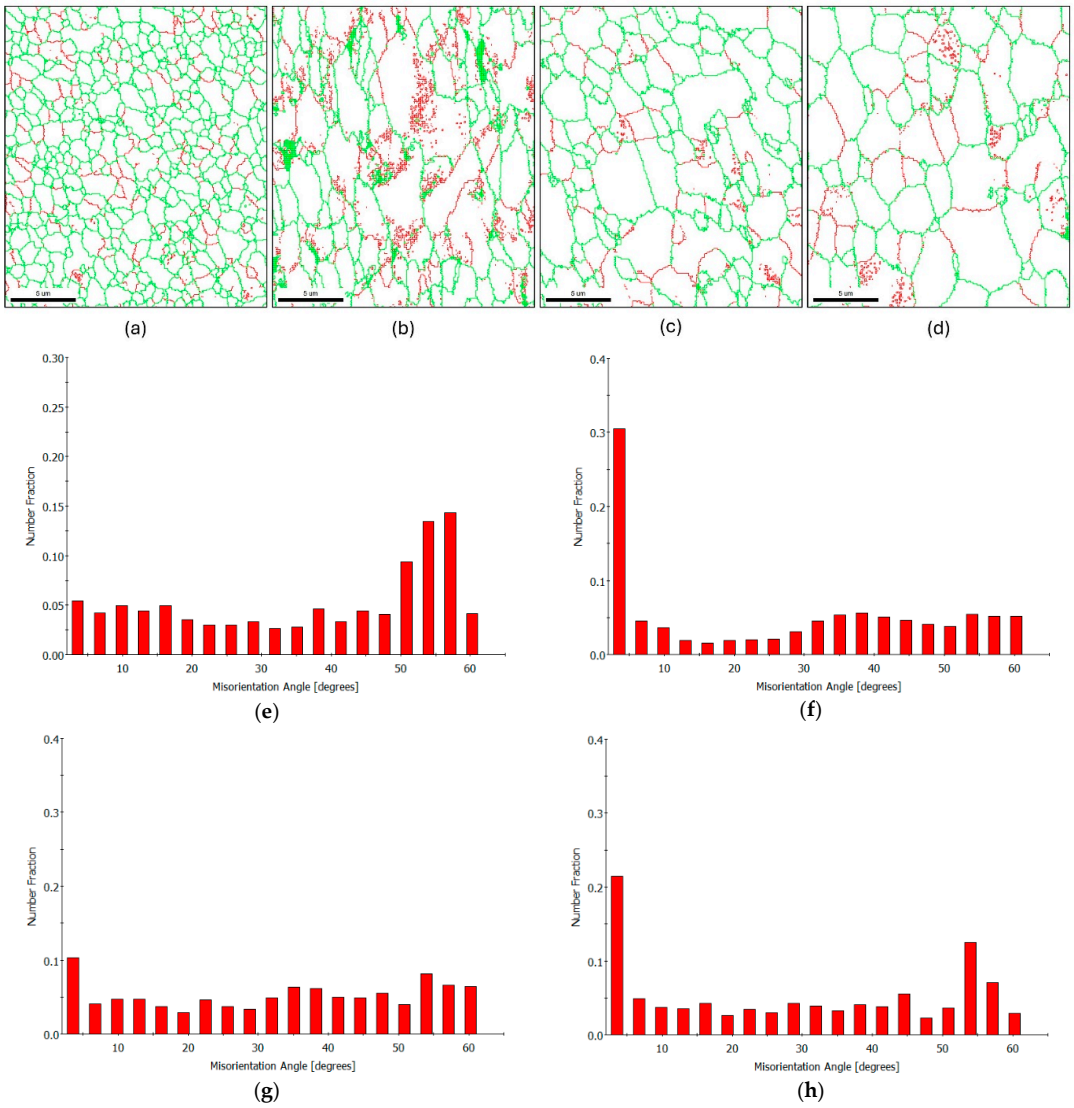

Figure 7. Grain boundary maps and corresponding misorientation angle histograms. (**a**,**e**) KOBO-processed, (**b**,**f**) KOBO-processed and annealed at 500 °C for 1 h, (**c**,**g**) KOBO-processed and annealed at 500 °C for 2 h, and (**d**,**h**) KOBO-processed and annealed at 500 °C for 3 h (red—low angle grain boundaries, green—high angle grain boundaries).

Figure 8 presents the CSL boundary map in which Σ3, Σ9, and Σ27 are represented by red, green, and black. As shown, in the KOBO-processed sample the fraction of Σ3 boundaries, which represent coherent twin boundaries, is relatively low, at 4.3%. The fractions of Σ9 and Σ27 boundaries, associated with higher-order twin boundaries, are minimal, each constituting only 0.1% of the total grain boundaries (Figure 8a).

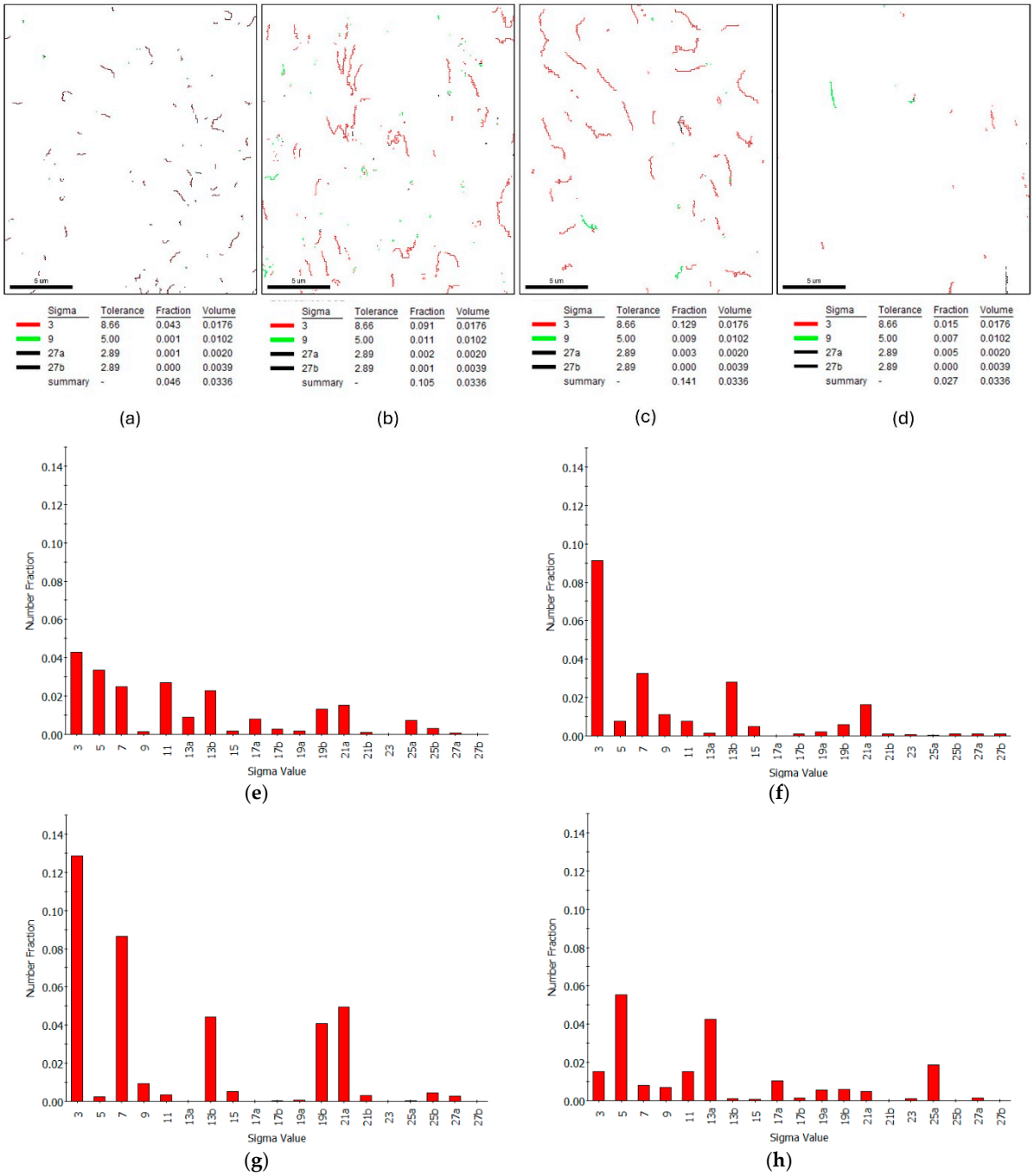

Figure 8. CSL boundary maps and corresponding histograms of CSL boundary distribution. (**a**,**e**) KOBO-processed sample, (**b**,**f**) KOBO-processed and annealed at 500 °C for 1 h, (**c**,**g**) KOBO-processed and annealed at 500 °C for 2 h, and (**d**,**h**) KOBO-processed and annealed at 500 °C for 3 h.

After annealing for 1 h at 500 °C, the fraction of Σ3 boundaries increased significantly to 9.1%, indicating the formation and stabilization of a higher number of twin boundaries

during the initial stages of recrystallization and grain growth (Figure 8b). The Σ9 and Σ27 boundaries also show a similar trend, with Σ9 rising to 1.1% and Σ27 to 0.3%.

A further increase in the Σ3 boundary fraction was observed in the sample annealed for 2 h. As shown in Figure 8c, the Σ3 boundary fraction reached its peak at 12.9%. In contrast, the Σ9 and Σ27 fractions remained relatively stable, at 0.9% and 0.3%, respectively.

After 3 h of annealing at 500 °C, the Σ3 boundary fraction dropped sharply to 1.5% (Figure 8d). This significant reduction is likely due to prolonged annealing, which accelerated grain growth. At this stage, the grains reach a critical size, allowing them to consume smaller surrounding grains with different orientations, resulting in a rapid decrease in Σ3 boundaries. Furthermore, the fractions of Σ9 and Σ27 boundaries decreased slightly, with Σ9 at 0.7% and Σ27 at 0.5%. These changes suggest that extended annealing promotes a more random distribution of grain boundary character, reducing the overall proportion of special grain boundaries.

To elucidate the mechanism of twin boundary evolution, texture analysis was performed by plotting the orientation distribution functions (ODFs). Table 2 summarizes the main texture components identified in the samples analyzed. The data clearly indicate that KOBO extrusion results in a texture characteristic of plane strain deformation processes. The primary texture components observed are Cube (indicative of dynamic recrystallization), along with Brass (heavily deformed alloys with low-to-medium SFEs develop strong brass textures owing to the formation of nanotwins [49]), S, R. Brass, and A. Notably, the annealing treatment led to an increase in the Brass texture component, which now accounts for approximately 55% of the total texture fraction. This development of the Brass component is likely attributable to the mechanism of strain-induced boundary migration (SIBM). During grain boundary migration, the Brass grains consume adjacent deformed grains, which subsequently transform into Brass grains due to the associated dislocation annihilation [50].

Table 2. Main texture components identified in the analyzed samples.

Texture Component	Cube {001}<100> (%)	Goss {011}<100> (%)	Brass {110}<112> (%)	Copper {112}<111> (%)	S {123}<634> (%)	R. Goss (RG) {011}<011> (%)	R. Brass (RB) {110}<556> (%)	A {112}<110> (%)
KOBO-processed	22.51	0.17	38.99	0.12	8.6	0.07	19.95	9.59
KOBO-processed and annealed at 500 °C for 1 h	3.31	0.74	54.75	2.01	13.21	1.6	2.91	21.46
KOBO-processed and annealed at 500 °C for 2 h	0.62	0.22	53.61	1.06	1.12	3.6	0.79	25.21
KOBO-processed and annealed at 500 °C for 3 h	32.53	0.97	8.72	0.36	0.85	33.74	0.25	6.62

Aiming to precisely analyze the texture evolution, the orientation distribution fraction maps were plotted. As can be seen in Figure 9a, the KOBO-processed sample exhibits the lowest texture intensity. Analysis of the ODF maps confirms a pronounced Brass {110}<112> component, a common orientation that typically develops during plane strain deformation, which emerged after the KOBO extrusion process. In addition to the Brass texture component, Cube {001}<100>, R. Brass {110}<556>, S {123}<634>, and A {112}<110> texture components were identified.

Annealing at 500 °C for 1 h did not significantly change the texture (Figure 9b). The primary texture components Brass, S, and A persisted; however, the volume fraction of the Brass {110}<112> component was significantly higher. This phenomenon of Brass enhancement during annealing was previously observed by Higginson et al. [51] in the AA1050 alloy and was attributed to strain-induced boundary migration (SIBM). From the CSL boundary map (Figure 8b), which shows an increase in the CSL boundary fraction, it can be

deduced that the composition and intensity of the Brass texture strongly correlate with the type and volume fraction of low-ΣCSL grain boundaries. According to Baudin et al. [52], a considerable difference in the accumulated deformation energy between {100} and {111} crystallites can be a stimulus for first-generation growth during annealing.

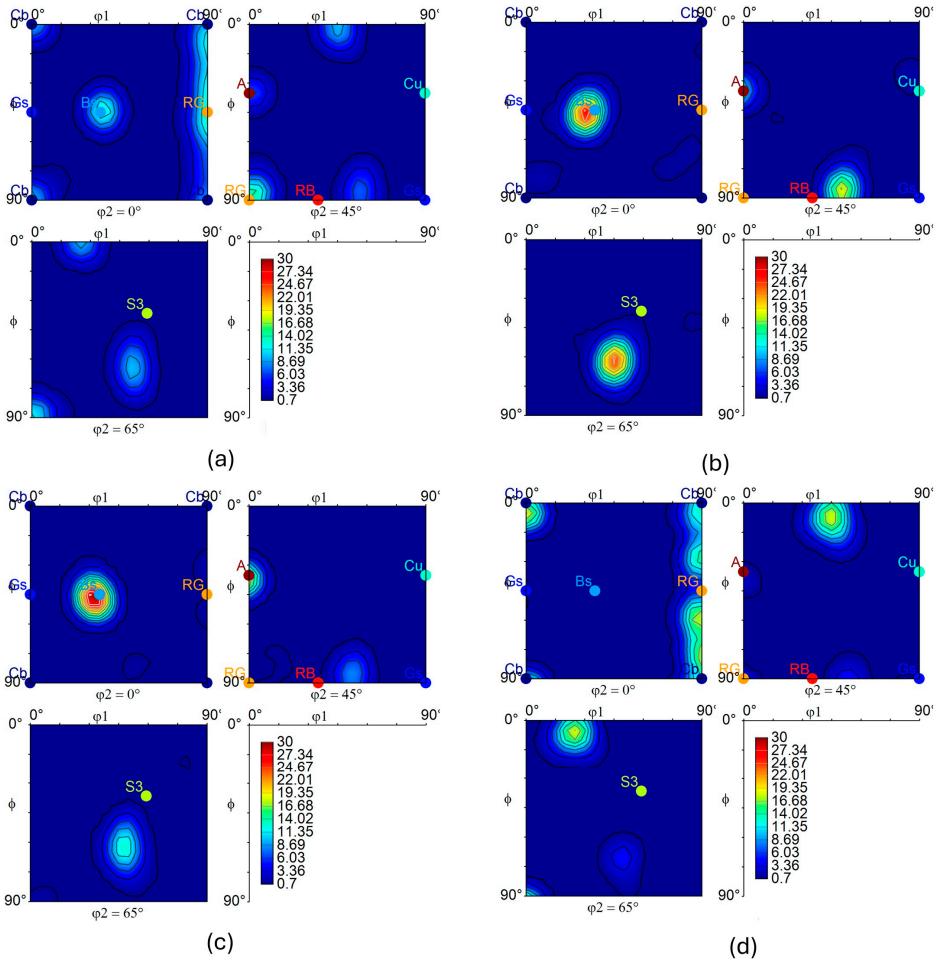

Figure 9. Experimental ODF maps. (**a**) KOBO-processed sample, (**b**) KOBO-processed and annealed at 500 °C for 1 h, (**c**) KOBO-processed and annealed at 500 °C for 2 h, and (**d**) KOBO-processed and annealed at 500 °C for 3 h.

After 2 h of annealing, a clear evolution in the texture components is observed (Figure 9c). The fractions of the A {112}<110> and R. Goss {110}<011> components increase, representing approximately 25% and 3.6% of the total texture, respectively. Meanwhile, the Brass {110}<112> component remains dominant, contributing 53% to the overall texture. Different substructural densities in different grain orientations are fundamental to this change in texture associated with this grain growth. The Brass-oriented grains must have a lower substructural energy density than the other main components for the texture change to occur by dynamic boundary migration [53].

The Cube and R. Goss textural components strengthen with increasing annealing time, while the Brass and A components weaken, as shown in Figure 9d. The presence of a Cube texture after annealing has been documented in several aluminum alloys [54,55], as it is a typical recrystallization texture. Zhao et al. [50] reported that Brass grains transform into Cube grains (Brass → Cube) during annealing. The evolution of Brass texture into recrystallization texture during annealing was studied by Huang et al. [56], who proposed the following transformation path: Brass texture → Goss texture → R. Goss texture → Cube texture. Considering the observed shift in the Brass to R. Goss texture ratio, it can be confirmed that the R. Goss grains have grown at the expense of Brass-oriented grains.

Furthermore, the high Cube texture and reduced Brass texture content contributed to a lower fraction of Σ3 CSL boundaries. A comparable trend was noted in a Cu-Ni alloy by Pen et al. [57], where an increase in annealing temperature led to an enhancement of Cube texture and a corresponding decrease in the twin boundary fraction.

Next, to clarify whether there is a correlation between the enhancement of the Brass texture and the CSL boundary fraction, texture component maps were superimposed on the EBSD grain boundary maps (Figure 10). Brass, $Brass_{45^\circ}$, $Brass_{70^\circ}$, m-Brass, and $Brass_{T1}$ orientations in the Euler space were defined according to Shen et al. [58].

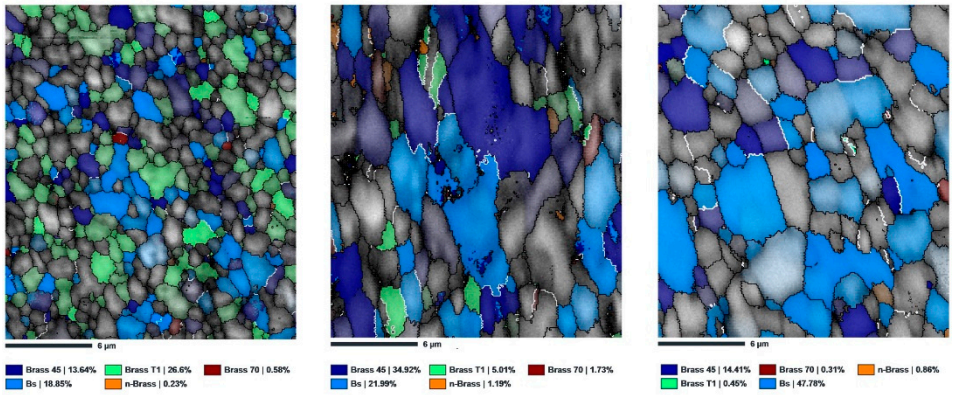

Figure 10. Brass texture components superimposed on the EBSD maps corresponding to (**a**) KOBO-processed, (**b**) KOBO-processed and annealed at 500 C for 1 h, and (**c**) KOBO-processed and annealed at 500 °C for 2 h samples. The white lines indicate Σ3 CSL boundaries, while the black lines represent boundaries having a misorientation angle greater than 5°.

As revealed in Figure 9a, a typical deformation texture, namely Brass, formed after the KOBO extrusion process. A more detailed examination of the Brass texture components, illustrated in Figure 10a, reveals the predominance of Brass, $Brass_{45^\circ}$, and $Brass_{T1}$ within the KOBO-processed sample microstructure. Previous studies [59,60] have reported the existence of a distinct 60°<1,−1,1> twin relationship between the $Brass_{45^\circ}$ and Brass components, as well as between Brass and $Brass_{T1}$. This unique texture evolution contributes to the increase in the fraction of Σ3 CSL twin boundaries, as revealed in Figure 8b.

The brass texture component was further enhanced after annealing at 500 °C for 1 h, indicating the appearance of strain-induced boundary migration driven by energy differentials between <111> and <100> grains. As shown in Figure 10b, this increase in the Σ3 CSL boundary fraction coincided with transformation of the Brass texture. Under these conditions, $Brass_{45^\circ}$ and Brass grains dominated the microstructure. The special rotational relationship along the <111> axis between Brass texture grains likely facilitated a preferential transformation pathway, promoting the observed texture evolution. This suggests that the <111> rotational alignment between Brass and its variants ($Brass_{45^\circ}$ and $Brass_{T1}$) plays a pivotal role in texture evolution during annealing [59,60]. There is also evidence in the literature supporting a correlation between Brass texture and CSL boundary formation. For instance, a study by Fang et al. [61] demonstrated that Σ3n grain clusters formed through the oriented growth of the Brass ({110}<112>) orientation.

With an extended annealing time of 2 h, the microstructure became dominated by Brass and $Brass_{45^\circ}$ grains, while other Brass texture components contributed only about 1% of the total texture fraction. Concurrently, the fraction of Σ3 CSL boundaries increased to approximately 12.9%. As observed in the texture component map (Figure 10c), these Σ3 boundaries predominantly separated the Brass and $Brass_{45^\circ}$ grains, confirming a correlation between the dominance of these texture components and the rise in Σ3 CSL boundary fraction.

Based on the findings above, it can be concluded that the Brass texture component can persist in the microstructure even after annealing. Additionally, the composition and

intensity of the Brass texture appear to be strongly correlated with the type and volume fraction of low-Σ CSL grain boundaries. Microstructural analysis indicates that an increase in the Brass texture component is associated with the growth of Brass-oriented grains. According to Samajdar et al. [62] the S/Brass/Goss grains have the lowest probability of encountering low-angle/low-mobility boundaries, but higher probability of possessing low-energy/CSL boundaries with higher mobility. Variable grain boundary mobility and energy, according to Rolett et al. [63], may also favor abnormal grain growth (AGG). Indeed, as shown in Figure 10c, Brass grains appear significantly larger than the surrounding matrix, indicating the early stages of AGG. Furthermore, as shown previously [64], the Σ3 boundaries in KOBO-processed samples are incoherent, and therefore exhibit much higher mobility compared with the coherent boundaries (twin boundaries). The migration and interactions of such incoherent Σ3 boundaries can yield Σ9 and even Σ27 boundaries. This may explain why the fraction of Σ9 boundaries increased during annealing. Further increasing the annealing time resulted in strengthening of the Cube texture component (Cube grains were recrystallized out of the parent Brass matrix), which is a typical recrystallization texture. This phenomenon was also detected by Alvi et al. [65], who found that Cube grains could slowly grow into deformed Brass matrix in 1050 alloy.

3.5. Effect of Annealing on Hardness

The changes in mechanical properties before and after annealing were evaluated through hardness measurements (Table 3). As shown, the hardness of the as-built LPBF sample is 117 HV. Such high hardness is due to the high dislocation density and fine cellular structure resulting from rapid solidification in the LPBF process. After annealing at 500 °C for 1 h, the hardness decreases significantly by ~50% to 61 HV and decreased further with longer annealing times. After 2 h at 500 °C, the hardness was 60 HV, and after 3 h at 500 °C, it reached 57 HV. This progressive softening correlates with the observed microstructural evolution presented in the manuscript. The KOBO-processed sample, which has a lower initial hardness of 92 HV, demonstrated better thermal stability compared to the LPBF sample. After annealing at 500 °C for 1 h, the hardness decreased only by 30% to ~64 HV; however, it had a hardness higher than that of the LPBF sample at the same temperature. Notably, after annealing for 2 h at 500 °C, the hardness was 62 HV, and after 3 h, it was 61 HV.

Table 3. Effect of annealing on hardness.

	Annealing time [h]			
	0	1	2	3
As-built	117 ± 1.8	61 ± 1.4	60 ± 1.5	57 ± 1.4
KOBO-processed	92 ± 2.1	64 ± 1.6	62 ± 1.4	61 ± 1.7

4. Conclusions

In this article, an AlSi10Mg alloy sample produced by selective laser melting was post-processed using the KOBO extrusion method and subsequently annealed to facilitate grain boundary engineering. The following conclusions can be drawn from the experimental results:

- Thermomechanical treatment resulted in significant grain refinement of the LPBF AlSi10Mg alloy microstructure, from ~3.6 μm to 0.8 μm.
- A special microstructure was produced by KOBO processing and subsequent annealing treatment, in which up to 44% of all boundaries were low-Σ CSL boundaries. The applied grain-boundary-engineering treatment increased the low-Σ3n CSL frequency from ~3.2% in the as-built condition to ~14.1% in the KOBO-processed sample annealed at 500 °C for 2 h.

- Strain-induced boundary migration (SIBM) was identified as the operative mechanism for the achievement of GBE microstructure in KOBO-processed LPBF AlSi10Mg alloy sample.
- After 2 h of annealing, Brass and $Brass_{45^\circ}$ grains dominated the microstructure, with the Σ3 CSL boundary fraction increasing to approximately 12.9%. The texture component map reveals that these boundaries primarily separate the Brass and $Brass_{45^\circ}$ grains, supporting the link between the Brass texture dominance and the rise in Σ3 CSL boundaries.
- Recrystallization resulted in the transformation of Brass {110}<112> texture into Cube {001}<100> texture. The Cube grains preferably grew in the Brass matrix after annealing for 3 h, resulting in a decrease in the Σ3n CSL boundary fraction.

Author Contributions: P.S.: conceptualization, methodology, validation, formal analysis, resources, data curation, writing—original draft, visualization, supervision, project administration, funding acquisition; L.L.: writing—original draft, J.B. writing—original draft, formal analysis. All authors have read and agreed to the published version of the manuscript.

Funding: The research was funded by the National Science Centre, Poland, based on decision number 2021/43/D/ST8/01946.

Data Availability Statement: Data are available on request.

Acknowledgments: This investigation was partially conducted within the framework of the Visegrad Fund International Scholarship received by Przemysław Snopiński for the period December 2024 to July 2025.

Conflicts of Interest: The authors declare no conflicts of interest.

References

1. Fathi, P.; Mohammadi, M.; Duan, X.; Nasiri, A.M. A Comparative Study on Corrosion and Microstructure of Direct Metal Laser Sintered AlSi10Mg_200C and Die Cast A360.1 Aluminum. *J. Mater. Process Technol.* **2018**, *259*, 1–14. [CrossRef]
2. Snopiński, P. Exploring Microstructure Refinement and Deformation Mechanisms in Severely Deformed LPBF AlSi10Mg Alloy. *J. Alloys Compd.* **2023**, *941*, 168984. [CrossRef]
3. Jandaghi, M.R.; Aversa, A.; Manfredi, D.; Calignano, F.; Lavagna, L.; Pavese, M. In Situ Alloying of AlSi10Mg-5 Wt% Ni through Laser Powder Bed Fusion and Subsequent Heat Treatment. *J. Alloys Compd.* **2022**, *904*, 164081. [CrossRef]
4. Liu, Y.J.; Liu, Z.; Jiang, Y.; Wang, G.W.; Yang, Y.; Zhang, L.C. Gradient in Microstructure and Mechanical Property of Selective Laser Melted AlSi10Mg. *J. Alloys Compd.* **2018**, *735*, 1414–1421. [CrossRef]
5. Alghamdi, F.; Haghshenas, M. Microstructural and Small-Scale Characterization of Additive Manufactured AlSi10Mg Alloy. *SN Appl. Sci.* **2019**, *1*, 255. [CrossRef]
6. Dong, Z.; Xu, M.; Guo, H.; Fei, X.; Liu, Y.; Gong, B.; Ju, G. Microstructural Evolution and Characterization of AlSi10Mg Alloy Manufactured by Selective Laser Melting. *J. Mater. Res. Technol.* **2022**, *17*, 2343–2354. [CrossRef]
7. Lefebvre, W.; Rose, G.; Delroisse, P.; Baustert, E.; Cuvilly, F.; Simar, A. Nanoscale Periodic Gradients Generated by Laser Powder Bed Fusion of an AlSi10Mg Alloy. *Mater. Des.* **2021**, *197*, 109264. [CrossRef]
8. Wu, J.; Wang, X.Q.; Wang, W.; Attallah, M.M.; Loretto, M.H. Microstructure and Strength of Selectively Laser Melted AlSi10Mg. *Acta Mater.* **2016**, *117*, 311–320. [CrossRef]
9. Di Egidio, G.; Ceschini, L.; Morri, A.; Martini, C.; Merlin, M. A Novel T6 Rapid Heat Treatment for AlSi10Mg Alloy Produced by Laser-Based Powder Bed Fusion: Comparison with T5 and Conventional T6 Heat Treatments. *Metall. Mater. Trans. B* **2022**, *53*, 284–303. [CrossRef]
10. Zhang, H.; Wang, Y.; Wang, J.J.; Ni, D.R.; Wang, D.; Xiao, B.L.; Ma, Z.Y. Achieving Superior Mechanical Properties of Selective Laser Melted AlSi10Mg via Direct Aging Treatment. *J. Mater. Sci. Technol.* **2022**, *108*, 226–235. [CrossRef]
11. Soe, A.N.; Sombatmai, A.; Promoppatum, P.; Srimaneepong, V.; Trachoo, V.; Pandee, P. Effect of Post-Processing Treatments on Surface Roughness and Mechanical Properties of Laser Powder Bed Fusion of Ti–6Al–4V. *J. Mater. Res. Technol.* **2024**, *32*, 3788–3803. [CrossRef]
12. Maleki, E.; Bagherifard, S.; Heydari Astaraee, A.; Sgarbazzini, S.; Bandini, M.; Guagliano, M. Application of Gradient Severe Shot Peening as a Novel Mechanical Surface Treatment on Fatigue Behavior of Additively Manufactured AlSi10Mg. *Mater. Sci. Eng. A* **2023**, *881*, 145397. [CrossRef]
13. Liu, Y.; Liu, X.; Lu, J.; Luo, K.; Zhang, Z.; Lu, H.; Zhang, H.; Xu, X.; Wang, Y.; Zhou, S. Post-Treatment Technologies for High-Speed Additive Manufacturing: Status, Challenge and Tendency. *J. Mater. Res. Technol.* **2024**, *30*, 1057–1082. [CrossRef]

14. Santos Macías, J.G.; Zhao, L.; Tingaud, D.; Bacroix, B.; Pyka, G.; van der Rest, C.; Ryelandt, L.; Simar, A. Hot Isostatic Pressing of Laser Powder Bed Fusion AlSi10Mg: Parameter Identification and Mechanical Properties. *J. Mater. Sci.* **2022**, *57*, 9726–9740. [CrossRef]
15. Wang, Y.; Shi, J. Effect of Hot Isostatic Pressing on Nanoparticles Reinforced AlSi10Mg Produced by Selective Laser Melting. *Mater. Sci. Eng. A* **2020**, *788*, 139570. [CrossRef]
16. Habibiyan, A.; Hanzaki, A.Z.; Abedi, H.R. An Investigation into Microstructure and High-Temperature Mechanical Properties of Selective Laser-Melted 316L Stainless Steel toward the Development of Hybrid Ampliforge Process. *Int. J. Adv. Manuf. Technol.* **2020**, *110*, 383–394. [CrossRef]
17. Gussev, M.N.; Sridharan, N.; Thompson, Z.; Terrani, K.A.; Babu, S.S. Influence of Hot Isostatic Pressing on the Performance of Aluminum Alloy Fabricated by Ultrasonic Additive Manufacturing. *Scr. Mater.* **2018**, *145*, 33–36. [CrossRef]
18. Liu, S.; Guo, H. Influence of Hot Isostatic Pressing (HIP) on Mechanical Properties of Magnesium Alloy Produced by Selective Laser Melting (SLM). *Mater. Lett.* **2020**, *265*, 127463. [CrossRef]
19. Finfrock, C.B.; Exil, A.; Carroll, J.D.; Deibler, L. Effect of Hot Isostatic Pressing and Powder Feedstock on Porosity, Microstructure, and Mechanical Properties of Selective Laser Melted AlSi10Mg. *Metallogr. Microstruct. Anal.* **2018**, *7*, 443–456. [CrossRef]
20. Valiev, R.Z.; Islamgaliev, R.K.; Alexandrov, I.V. Bulk Nanostructured Materials from Severe Plastic Deformation. *Prog. Mater. Sci.* **2000**, *45*, 103–189. [CrossRef]
21. Mohd Yusuf, S.; Chen, Y.; Yang, S.; Gao, N. Micromechanical Response of Additively Manufactured 316L Stainless Steel Processed by High-Pressure Torsion. *Adv. Eng. Mater.* **2020**, *22*, 2000052. [CrossRef]
22. Snopiński, P.; Matus, K.; Tatiček, F.; Rusz, S. Overcoming the Strength-Ductility Trade-off in Additively Manufactured AlSi10Mg Alloy by ECAP Processing. *J. Alloys Compd.* **2022**, *918*, 165817. [CrossRef]
23. You, Z.Y.; Tang, Z.Y.; Chu, F.B.; Ding, H.; Misra, R.D.K. Significantly Enhancing Elevated-Temperature Strength and Ductility of a FeMnCoCr High-Entropy Alloy via Grain Boundary Engineering: Exploring Multi-Deformation Mechanisms. *Mater. Sci. Eng. A* **2023**, *886*, 145547. [CrossRef]
24. Zhang, Y.-Q.; Quan, G.-Z.; Zhao, J.; Yu, Y.-Z.; Xiong, W. A Review on Controlling Grain Boundary Character Distribution during Twinning-Related Grain Boundary Engineering of Face-Centered Cubic Materials. *Materials* **2023**, *16*, 4562. [CrossRef]
25. Zhang, C.; Lin, L.; Chen, R.; Zhang, L.; Shao, Z. Grain Boundary Engineering and Its Effect on Intergranular Corrosion Resistance of a Ni-Cr-Mo Based C276 Superalloy. *Crystals* **2022**, *12*, 1625. [CrossRef]
26. Athreya, C.N.; Deepak, K.; Kim, D.-I.; de Boer, B.; Mandal, S.; Subramanya Sarma, V. Role of Grain Boundary Engineered Microstructure on High Temperature Steam Oxidation Behaviour of Ni Based Superalloy Alloy 617. *J. Alloys Compd.* **2019**, *778*, 224–233. [CrossRef]
27. Zhang, B.B.; Tang, Y.G.; Mei, Q.S.; Li, X.Y.; Lu, K. Inhibiting Creep in Nanograined Alloys with Stable Grain Boundary Networks. *Science* **2022**, *378*, 659–663. [CrossRef] [PubMed]
28. Guan, X.J.; Shi, F.; Ji, H.M.; Li, X.W. A Possibility to Synchronously Improve the High-Temperature Strength and Ductility in Face-Centered Cubic Metals through Grain Boundary Engineering. *Scr. Mater.* **2020**, *187*, 216–220. [CrossRef]
29. Taali, S.; Toroghinejad, M.R.; Kuglstatter, M.; Höppel, H.W. Grain Boundary Engineering in Roll-Bonded Copper to Overcome the Strength-Ductility Dilemma. *J. Mater. Res. Technol.* **2022**, *17*, 3198–3204. [CrossRef]
30. Mao, Q.; Zhang, M.; Zhi, Y.; Wang, C.; Li, H. Improve the Ductility of a Nickel Based Superalloy by Optimizing Secondary Phase Distribution through Grain Boundary Engineering. *Mater. Charact.* **2021**, *181*, 111510. [CrossRef]
31. Liu, B.; Zhang, H.; Xu, J.; Gao, Y.; Yang, X.; Zhen, B.; Hu, Y.; Ding, Y.; Zhang, D.; Lu, S. Improving the Hot Corrosion Resistance of Additively Manufactured Inconel 718 via Recrystallization-Based Grain Boundary Engineering Induced by Its Residual Stress. *Mater. Today Commun.* **2024**, *39*, 108792. [CrossRef]
32. Gao, S.; Hu, Z.; Duchamp, M.; Krishnan, P.S.S.R.; Tekumalla, S.; Song, X.; Seita, M. Recrystallization-Based Grain Boundary Engineering of 316L Stainless Steel Produced via Selective Laser Melting. *Acta Mater.* **2020**, *200*, 366–377. [CrossRef]
33. Zhang, Y.; Lin, W.; Zhai, Z.; Wu, Y.; Yang, R.; Zhang, Z. Enhancing the Mechanical Property of Laser Powder Bed Fusion CoCrMo Alloy by Tailoring the Microstructure and Phase Constituent. *Mater. Sci. Eng. A* **2023**, *862*, 144449. [CrossRef]
34. Zhang, H.; Li, B.; Hu, J.; Qian, G.; Li, C. Experimental Investigation on the Deformation Behavior of an Isotropic 304L Austenitic Steel Manufactured by Laser Powder Bed Fusion with Hot Isostatic Pressing. *Mater. Charact.* **2024**, *214*, 114086. [CrossRef]
35. Pei, C.; Yuan, H.; Li, B.; Ma, S. Anisotropic Damage Evolution and Modeling for a Nickel-Based Superalloy Built by Additive Manufacturing. *Eng. Fract. Mech.* **2022**, *268*, 108450. [CrossRef]
36. Seita, M.; Gao, S. Broadening the Design Space of Engineering Materials through "Additive Grain Boundary Engineering". *J. Mater. Sci.* **2022**, *57*, 9530–9540. [CrossRef]
37. Song, L.; Zhao, L.; Ding, L.; Zhu, Y.; Huang, M.; Simar, A.; Li, Z. Microstructure and Loading Direction Dependent Hardening and Damage Behavior of Laser Powder Bed Fusion AlSi10Mg. *Mater. Sci. Eng. A* **2022**, *832*, 142484. [CrossRef]
38. Eom, Y.S.; Park, J.M.; Choi, J.-W.; Seong, D.-J.; Joo, H.; Jo, Y.C.; Kim, K.T.; Yu, J.H.; Son, I. Fine-Tuning of Mechanical Properties of Additively Manufactured AlSi10Mg Alloys by Controlling the Microstructural Heterogeneity. *J. Alloys Compd.* **2023**, *956*, 170348. [CrossRef]
39. Bao, J.; Wu, Z.; Wu, S.; Withers, P.J.; Li, F.; Ahmed, S.; Benaarbia, A.; Sun, W. Hot Dwell-Fatigue Behaviour of Additively Manufactured AlSi10Mg Alloy: Relaxation, Cyclic Softening and Fracture Mechanisms. *Int. J. Fatigue* **2021**, *151*, 106408. [CrossRef]

40. de Sonis, E.; Dépinoy, S.; Giroux, P.-F.; Maskrot, H.; Lemarquis, L.; Hercher, O.; Villaret, F.; Gourgues-Lorenzon, A.-F. Dependency of Recrystallization Kinetics on the Solidification Microstructure of 316L Stainless Steel Processed by Laser Powder Bed Fusion (LPBF). *Mater. Charact.* **2022**, *194*, 112370. [CrossRef]
41. Snopiński, P. Effects of KoBo-Processing and Subsequent Annealing Treatment on Grain Boundary Network and Texture Development in Laser Powder Bed Fusion (LPBF) AlSi10Mg Alloy. *Symmetry* **2024**, *16*, 122. [CrossRef]
42. Yin, W.; Wang, W.; Fang, X.; Qin, C.; Xing, X. Migration of Grain Boundaries and Triple Junctions in High-Purity Aluminum during Annealing after Slight Cold Rolling. *Mater. Charact.* **2015**, *107*, 134–138. [CrossRef]
43. Snopiński, P.; Matus, K. Characterisation of Microstructure and Special Grain Boundaries in LPBF AlSi10Mg Alloy Subjected to the KoBo Extrusion Process. *Symmetry* **2023**, *15*, 1634. [CrossRef]
44. Beausir, B.; Fundenberger, J.J. *Analysis Tools for Electron and X-Ray Diffraction*; ATEX—Software 2007; Université de Lorraine-Metz: Metz, France, 2007.
45. Sabzi, H.E.; Hernandez-Nava, E.; Li, X.-H.; Fu, H.; San-Martín, D.; Rivera-Díaz-del-Castillo, P.E.J. Strengthening Control in Laser Powder Bed Fusion of Austenitic Stainless Steels via Grain Boundary Engineering. *Mater. Des.* **2021**, *212*, 110246. [CrossRef]
46. Liu, B.; Ding, Y.; Xu, J.; Gao, Y.; Chu, C.; Hu, Y.; Chen, D. Grain Boundary Engineering Activated by Residual Stress during the Laser Powder Bed Fusion of Inconel 718 and the Electrochemical Corrosion Performance. *Mater. Charact.* **2023**, *204*, 113160. [CrossRef]
47. Cui, X.; Zhang, S.; Wang, Z.Y.; Zhang, C.H.; Ni, C.L.; Wu, C.L. Microstructure and Fatigue Behavior of 24CrNiMo Low Alloy Steel Prepared by Selective Laser Melting. *Mater. Sci. Eng. A* **2022**, *845*, 143215. [CrossRef]
48. Mei, J.; Han, Y.; Sun, J.; Jiang, M.; Zu, G.; Song, X.; Zhu, W.; Ran, X. Improving the Comprehensive Mechanical Property of the AlSi10Mg Alloy via Parameter Adaptation of Selective Laser Melting and Heat Treatment. *J. Alloys Compd.* **2024**, *981*, 173623. [CrossRef]
49. Bhattacharjee, P.P.; Sathiaraj, G.D.; Zaid, M.; Gatti, J.R.; Lee, C.; Tsai, C.-W.; Yeh, J.-W. Microstructure and Texture Evolution during Annealing of Equiatomic CoCrFeMnNi High-Entropy Alloy. *J. Alloys Compd.* **2014**, *587*, 544–552. [CrossRef]
50. Zhao, Q.; Liu, Z. Texture Evolution of Hot Rolled Al–Cu–Mg–Zr Alloy During Annealing. *Met. Mater. Int.* **2022**, *28*, 2947–2961. [CrossRef]
51. Higginson, R.; Bate, P. Substructure Drag Effects and Recrystallization Textures in Aluminium. *Acta Mater.* **1999**, *47*, 1079–1090. [CrossRef]
52. Baudin, T.; Etter, A.L.; Penelle, R. Annealing Twin Formation and Recrystallization Study of Cold-Drawn Copper Wires from EBSD Measurements. *Mater. Charact.* **2007**, *58*, 947–952. [CrossRef]
53. Bate, P.S.; Huang, Y.; Humphreys, F.J. Development of the "Brass" Texture Component during the Hot Deformation of Al–6Cu–0.4Zr. *Acta Mater.* **2004**, *52*, 4281–4289. [CrossRef]
54. Liu, W.C.; Zhai, T.; Morris, J.G. Comparison of Recrystallization and Recrystallization Textures in Cold-Rolled DC and CC AA 5182 Aluminum Alloys. *Mater. Sci. Eng. A* **2003**, *358*, 84–93. [CrossRef]
55. Kumar, R.; Gupta, A.; Dandekar, T.R.; Khatirkar, R.K. Microstructure and Texture Development in AA3003 Aluminium Alloy. *Mater. Today Commun.* **2020**, *24*, 100965. [CrossRef]
56. Huang, T.; Liu, F.; Liu, Z.; He, G. Evolution of Microstructure, Texture, and Hardness in an Al-Cu-Mg Alloy during Annealing. *J. Mater. Eng. Perform.* **2022**, *31*, 1419–1431. [CrossRef]
57. Chen, X.P.; Sun, H.F.; Chen, D.; Wang, L.X.; Liu, Q. On Recrystallization Texture and Magnetic Property of Cu-Ni Alloys. *Mater. Charact.* **2016**, *121*, 149–156. [CrossRef]
58. Shen, F.; Sun, Z.; Li, W.; Zhou, Z.; Zhong, S.; Huang, H.; Guo, J.; Xie, C.; Wang, Y.; Yi, D. Texture Evolution in Hot-Rolled Al–Cu–Mg Sheets Using Orientation Streamline Approach and Texture Index. *J. Alloys Compd.* **2020**, *816*, 152415. [CrossRef]
59. Shen, F.; Sun, Z.; Li, W.; Zhou, Z.; Guo, J.; Hai, Y.; Zhao, Y.; Zhang, Y.; Luo, J.; Deng, Y.; et al. New Insight of Texture and Microstructure Evolution, and the Connections between with Tensile Performance in as-Annealed Al-Cu-Mg-Zr Sheet. *J. Alloys Compd.* **2023**, *967*, 171784. [CrossRef]
60. Shen, F.; Li, W.; Sun, Z.; Zhou, Z.; Xie, C.; Liao, Z.; Yi, D. Insights of Texture and Microstructure Evolution in the Short Time Annealing of Al-Cu-Mg Alloy at Large Temperature Range. *J. Alloys Compd.* **2021**, *871*, 159613. [CrossRef]
61. Fang, X.; Liu, Z.; Tikhonova, M.; Belyakov, A.; Wang, W. Evolution of texture and development of Σ3n grain clusters in 316 austenitic stainless steel during thermal mechanical processing. *J. Mater. Sci.* **2013**, *48*, 997–1004. [CrossRef]
62. Samajdar, I.; Rabet, L.; Verlinden, B.; Van Houtte, P. An Investigation on Grain Growth in a Commercial Al–Mg Alloy. *Texture Stress Microstruct.* **1998**, *30*, 314096. [CrossRef]
63. Rollett, A.D.; Mullins, W.W. On the Growth of Abnormal Grains. *Scr. Mater.* **1997**, *36*, 975–980. [CrossRef]
64. Snopiński, P.; Matus, K.; Łagoda, M.; Appiah, A.N.S.; Hajnyš, J. Engineering an Ultra-Fine Grained Microstructure, Twins and Stacking Faults in PBF-LB/M Al-Si Alloy via KoBo Extrusion Method. *J. Alloys Compd.* **2024**, *970*, 172576. [CrossRef]
65. Alvi, M.H.; Cheong, S.W.; Suni, J.P.; Weiland, H.; Rollett, A.D. Cube Texture in Hot-Rolled Aluminum Alloy 1050 (AA1050)—Nucleation and Growth Behavior. *Acta Mater.* **2008**, *56*, 3098–3108. [CrossRef]

Disclaimer/Publisher's Note: The statements, opinions and data contained in all publications are solely those of the individual author(s) and contributor(s) and not of MDPI and/or the editor(s). MDPI and/or the editor(s) disclaim responsibility for any injury to people or property resulting from any ideas, methods, instructions or products referred to in the content.